Petroleum Science 23 (2026) 1182–1196

Contents lists available at ScienceDirect

Petroleum Science

journal homepage: www.keaipublishing.com/en/journals/petroleum-science

Original Paper

Irregularly seismic data interpolation based on deep learning with integrated channel-spatial attention mechanism

Chao Ma [a], Jian-Ping Huang [a,*], Zi-Xuan Qiao [a], San-Fu Li [b], Wen-Sheng Duan [c], Gang-Lin Lei [c]

[a] State Key Laboratory of Deep Oil and Gas, School of Geosciences, China University of Petroleum (East China), Qingdao, 266580, Shandong, China
[b] Institute of Geophysical Exploration, Geophysical-China Oilfield Services Limit, Zhanjiang, 524057, Guangdong, China
[c] Tarim Oilfield Branch, CNPC, Korla, 841000, Xinjiang, China

ARTICLE INFO

Article history:
Received 20 April 2025
Received in revised form
26 June 2025
Accepted 9 October 2025
Available online 11 October 2025

Edited by Meng-Jiao Zhou

Keywords:
Seismic data
Deep learning
Irregular sampling
Channel-spatial attention mechanism
Interpolation

ABSTRACT

To address the challenges of irregular sampling and insufficient spatial sampling in field seismic data, this study proposed a deep learning-based interpolation method incorporating dual channel spatial attention mechanisms (CSAM). The proposed model establishes a collaborative framework of channel and spatial attention, enhancing feature representation by establishing connections between local reflection characteristics and global structural features. The performance of the method was evaluated through synthetic data experiments, including sparsity sensitivity tests, noise sensitivity tests, and field data validation, using metrics such as signal to noise ratio (SNR), mean absolute error (MAE), and structural similarity index (SSIM). Comparative analyses were conducted with Fourier projection onto convex sets (Fourierpocs), the classic U-net, and the efficient channel attention U-net (ECAUnet). Results demonstrate that the proposed method outperforms existing methods in reconstructing seismic reflection events and preserving amplitude fidelity, particularly in scenarios with extensive random data missing.

1. Introduction

Economic, environmental, equipment-related constraints often result in poor and irregular spatial sampling of seismic data. Most state-of-the-art seismic processing algorithms, such as full waveform inversion (Li and Alkhalifah, 2022), least-squares reverse time migration (Huang et al., 2023), heavily rely on high-quality, regularly sampled data. Therefore, reconstructing missing seismic data during the preprocessing stage is a critical yet challenging task. Currently, there are two major types of methods for seismic data interpolation and reconstruction: theory-driven and data-driven. Based on different underlying assumptions, there are four categories of theory-driven methods. The first category comprises model-driven techniques, which rely on simplified assumptions about the subsurface velocity model to perform an implicit migration-demigration process (Ronen, 1987; Stolt, 2002; Fomel, 2003). These methods can handle both random and regular missing data but exhibit significant performance degradation under complex geological conditions. The second category models seismic data as a (local) superposition of plane waves (Brandolin et al., 2024), and employs predictive filters for interpolation (Spitz, 1991; Porsani, 1999; Naghizadeh and Sacchi, 2007). Although this approach is effective for regularly sampled data, its interpolation performance heavily depends on the selection of the window size, which is challenging to optimize (Wang et al., 2019). The third category leverages the low-rank characteristics of seismic data by reformulating the interpolation problem as a rank-reduction or matrix completion problem (Trickett, 2003; Oropeza and Sacchi, 2011; Ma, 2013; Adamo et al., 2015; Siahsar et al., 2017). These methods are suitable for linear or quasi-linear events and are robust to noise and missing traces. However, the selection of the rank parameter typically relies on an approximate analysis of linear events in local windows. The fourth category assumes that seismic data exhibit sparse representations in a certain transform domain and imposes sparsity constraints for interpolation (Herrmann and Hennenfent, 2008; Ma and Plonka, 2010; Ma, 2010; Naghizadeh, 2012; Gan et al., 2015; Wang, 2016;

* Corresponding author.
E-mail address: jphuang@upc.edu.cn (J.-P. Huang).
Peer review under the responsibility of China University of Petroleum (Beijing).

https://doi.org/10.1016/j.petsci.2025.10.004

Zhang et al., 2020). The strength of these methods lies in their ability to represent data effectively with a few nonzero transform coefficients. However, their success depends on the selection of an appropriate transform basis and typically assumes that events are linear (Niu et al., 2021). Despite the good performance of theory-driven methods in seismic trace interpolation tasks, they share some common limitations when reconstructing missing traces. For instance, the performance of these algorithms heavily relies on the accuracy of prior information, and incorrect priors can lead to misjudgment of the problem model, thereby compromising the reliability of the results. Moreover, traditional methods are often computationally slow and lack generalizability; algorithms designed for specific datasets frequently require readjustment or modification when applied to new data types.

Deep learning has achieved remarkable success in fields such as medical image segmentation, computer vision, and natural language processing. Researchers have successfully introduced deep learning into the field of geophysics (Jia and Ma, 2017; Wu et al., 2023), yielding promising results in applications. Wu et al. (2019a, 2019b) proposed advanced convolutional neural network based methods, including FaultSeg3D, FaultNet3D, and realistic structural model training, to enhance 3D seismic fault segmentation, fault property prediction, and structural interpretation using both synthetic and realistic datasets (Wu et al., 2020, 2021). Luo et al. (2023, 2024) proposed multitask deep learning approaches for seismic data processing, including strata boundary-constrained multihorizon tracking and two-stage separation of strong and weak reflections, to enhance seismic interpretation and analysis. Zhu et al. (2019) proposed a deep neural network based approach for seismic signal denoising and decomposition, improving the quality and interpretation of seismic data. Li et al. (2024) proposed a conditional denoising diffusion probabilistic model for ground-roll attenuation, enhancing seismic data quality and processing efficiency. Zhang et al. (2024) proposed a conditional denoising diffusion probabilistic model for seismic diffraction separation and imaging, improving the accuracy of seismic interpretation and imaging processes.

Seismic data interpolation using deep learning has garnered widespread attention and application as a promising solution to the limitations of traditional interpolation methods (Wang et al., 2019; Sun et al., 2020). Models such as convolutional neural networks (CNNs), generative adversarial networks (GANs), and convolutional autoencoders have demonstrated the ability to learn complex mapping relationships from data. Data-driven deep learning approaches, often leveraging autoencoder, automatically extract spatial and temporal features from data, thereby reducing reliance on prior assumptions. The U-net is a specially designed autoencoder, it inherits the encoder-decoder structure of traditional autoencoder. Its unique skip connections between the encoder and decoder enable the decoder to simultaneously utilize high-level semantic features and low-level detailed information. For seismic data interpolation tasks (Jaderberg et al., 2015; Li et al., 2021; Liu et al., 2021; Dou et al., 2023), autoencoder-based methods employ encoders to extract latent variables from incomplete data, while decoders, supervised by complete data, generate reconstructed seismic data. While this end-to-end learning approach is effective, it has limitations in capturing global information, resulting in models that are strong in local feature extraction but weaker in global feature representation.

In recent years, attention mechanisms have become an indispensable component of deep learning architectures, particularly in the field of computer vision. They have proven to be highly valuable in identifying and emphasizing important regions in images (Mnih et al., 2014; Bahdanau et al., 2014; Xu et al., 2015; Yu and Wu, 2021), enabling dynamic and adaptive adjustment of focus based on input sequences. To address the limitations of autoencoder methods in capturing global information, attention mechanisms have recently been introduced into seismic data interpolation tasks, with researchers integrating them into various network architectures. For instance, Chai et al. (2020) embedded a channel attention module into a U-net for feature modeling. He et al. (2021) employed a multi-stage training process to train multiple U-net models, each focusing on interpolating missing components within different amplitude ranges, achieving promising interpolation results. Li et al. (2021) introduced a coordinate attention module into a U-net for 2D continuous missing trace interpolation, resulting in more accurate and reasonable interpolation outcomes. Shan et al. (2021) proposed a multi-stage U-net to progressively interpolate continuously missing seismic lines. Cheng et al. (2023) and Guo et al. (2023) utilized the self-attention mechanism of Transformers to capture long-range dependencies, thereby more accurately restoring the detailed information of missing data. For seismic data, spatial continuity manifests as strong correlations between signals from adjacent traces, while different frequency components carry information about subsurface geological structures at varying scales (high frequencies correspond to thin-layer details, and low frequencies represent thick-layer or basement features). The intensity of amplitudes directly reflects differences in reflection coefficients at geological interfaces. When seismic data slices serve as network inputs, the channel dimension represents a stack of filters learned by convolutional layers to respond to various seismic event characteristics, and the spatial dimension characterizes the positional distribution of reflection features within the seismic data slice. However, channel attention mechanisms typically focus solely on channel-wise information, ignoring the interplay between channels and spatial dimensions. This limitation restricts the model's ability to capture globally complex spatial features and establish connections between localized reflection features and overarching geological structures. Based on this, this study introduces channel and spatial attention mechanisms, proposing a deep learning interpolation method. The model dynamically captures channel and spatial features from the input seismic data, thereby enhancing the reconstruction capability for missing seismic traces. Through sparsity sensitivity tests and noise sensitivity tests on synthetic datasets, as well as tests on marine seismic data and field data, combined with quantitative and qualitative evaluation metrics, the proposed method was compared with traditional Fourier projection onto convex sets (Fourierpocs), the classical U-net, and the improved efficient channel attention U-net (ECAUnet). The experimental results demonstrate that the proposed method exhibits significant advantages in seismic reflection event reconstruction and amplitude fidelity, along with robust noise resistance, highlighting its strong applicability and potential.

2. Methods

2.1. Channel and spatial attention mechanism block

For the seismic data interpolation task, our objective is to design an attention mechanism that enhances the connection between local reflection features of missing traces and global geological structures. Inspired by convolutional block attention module (Woo et al., 2018), the submodules were redesigned and the workflow is illustrated in Fig. 1. Given an intermediate feature map $Y \in \mathbb{R}^{B\times C\times H\times W}$, where B denotes the batch size, representing the number of samples per batch, C denotes the number of feature map channels, H represents the height, and W represents the width of the feature map. Thus, the feature map constitutes a four-dimensional tensor. Each position (b, c, h, w) (with $b = 1, \ldots, B$;

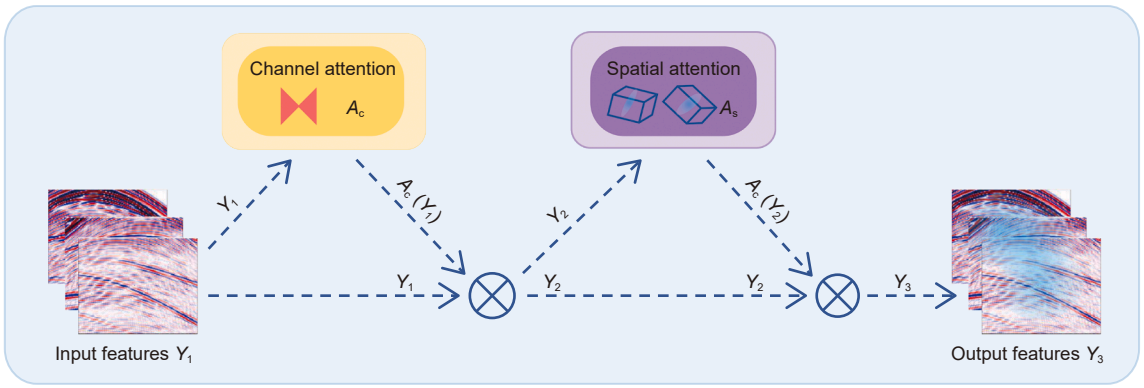

Fig. 1. The overview of channel-spatial attention mechanism block. The block has two sequential submodules: the channel attention and the spatial attention. The intermediate feature map is adaptively refined through this module in every convolutional block of the deep neural network.

$c = 1, \ldots, C$; $h = 1, \ldots, H$; $w = 1, \ldots, W$) contains a corresponding feature response value.

As illustrated in Fig. 1, by taking the intermediate feature map $Y_1 \in \mathbb{R}^{B\times C\times H\times W}$ as input, the module sequentially generates two types of attention maps, one is a channel attention map $A_c \in \mathbb{R}^{B\times C\times 1\times 1}$, where B denotes the batch size, representing the number of samples in the current batch, the second dimension C denotes the number of feature map channels (each channel in the input feature map has a corresponding attention weight for every sample), and the last two dimensions are both 1, indicating that spatial positions in the feature map are disregarded, with focus exclusively on information within the channel dimension. The other is a spatial attention map $A_s \in \mathbb{R}^{B\times 1\times H\times W}$, where B denotes the batch size, representing the number of samples in the current

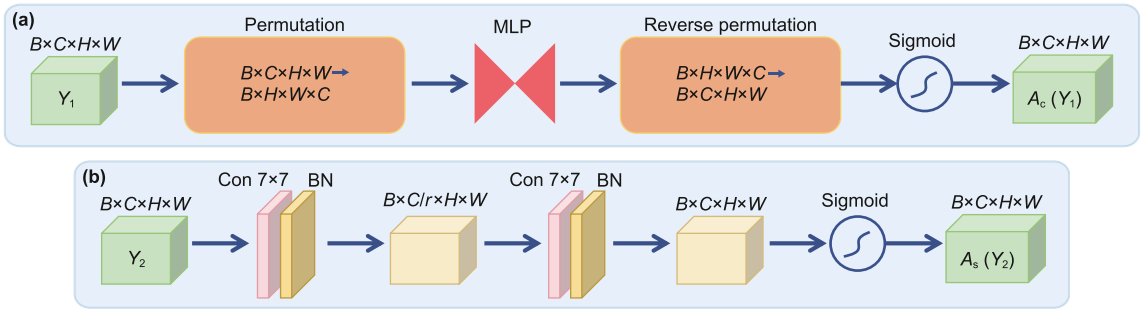

Fig. 2. Channel attention submodule of **(a)** and spatial attention submodule of **(b)**.

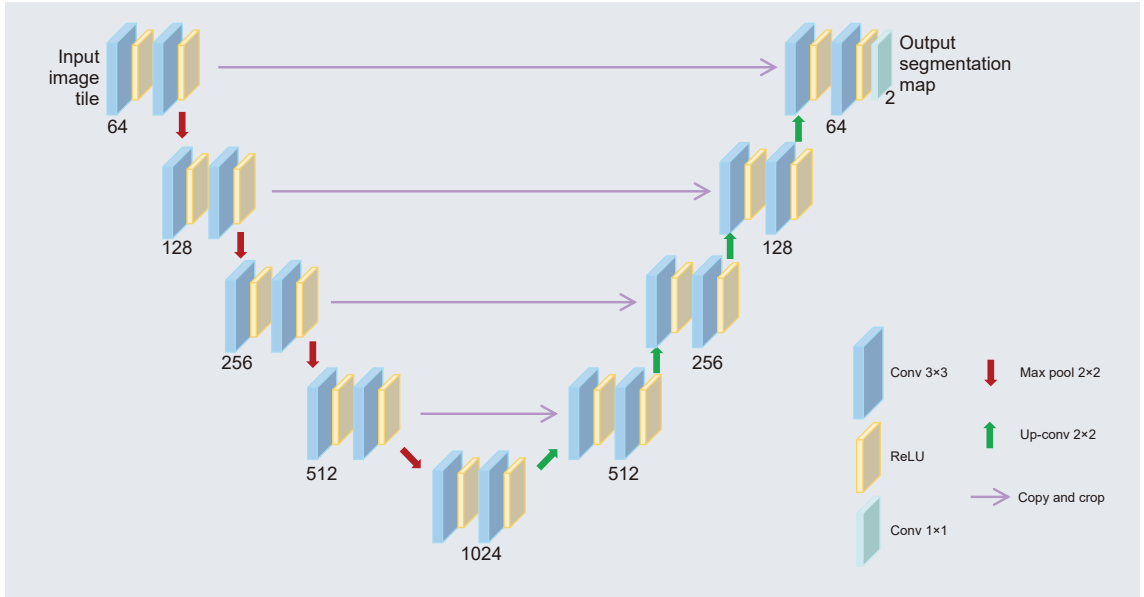

Fig. 3. The U-net architecture (modified after Rnneberger et al., 2015).

batch, corresponds to a distinct spatial attention map for each sample in the batch, the second dimension is 1, indicating that channel information is aggregated, while the last two dimensions H and W align with the height and width of the input feature map, respectively, emphasizing attention over spatial locations across the feature map. The overall attention computation process can be described by Eqs. (1) and (2):

$$Y_2 = A_c(Y_1) \otimes Y_1 \tag{1}$$

$$Y_3 = A_s(Y_2) \otimes Y_2 \tag{2}$$

where, A_c and A_s represent the channel attention map and the spatial attention map, $\otimes$ denotes element-wise multiplication, and Y_3 is final optimized output.

2.1.1. Channel attention submodule

The workflow of the channel attention submodule is illustrated in Fig. 2(a). This submodule employs dimension transformation to preserve information across different dimensions and leverages inter-channel relationships of features to generate a channel attention map. Its core consists of a multilayer perceptron (MLP) with two linear layers. The input feature Y_1 is first reshaped into a four-dimensional arrangement of batch size × channel × height × width ($B \times C \times H \times W$). Subsequently, the feature passes through the first linear layer of the MLP, which reduces the channel dimension to C/r, where r denotes the reduction ratio, defaulting to 4. The purpose of the reduction ratio is to decrease the channel dimension while preserving key features. This design is based on a comprehensive consideration of computational efficiency, feature representation capability, and experimental validation. If the reduction ratio r is too small, the number of channels after reduction remains large, leading to high computational costs. Conversely, if r is too large, the number of channels after reduction becomes too small, potentially causing the loss of important information. The default value in practical applications effectively compresses channel information, removes redundant features, and retains crucial ones, achieving an optimal balance between computational efficiency and feature representation capability. Afterward, the feature undergoes processing by the second linear

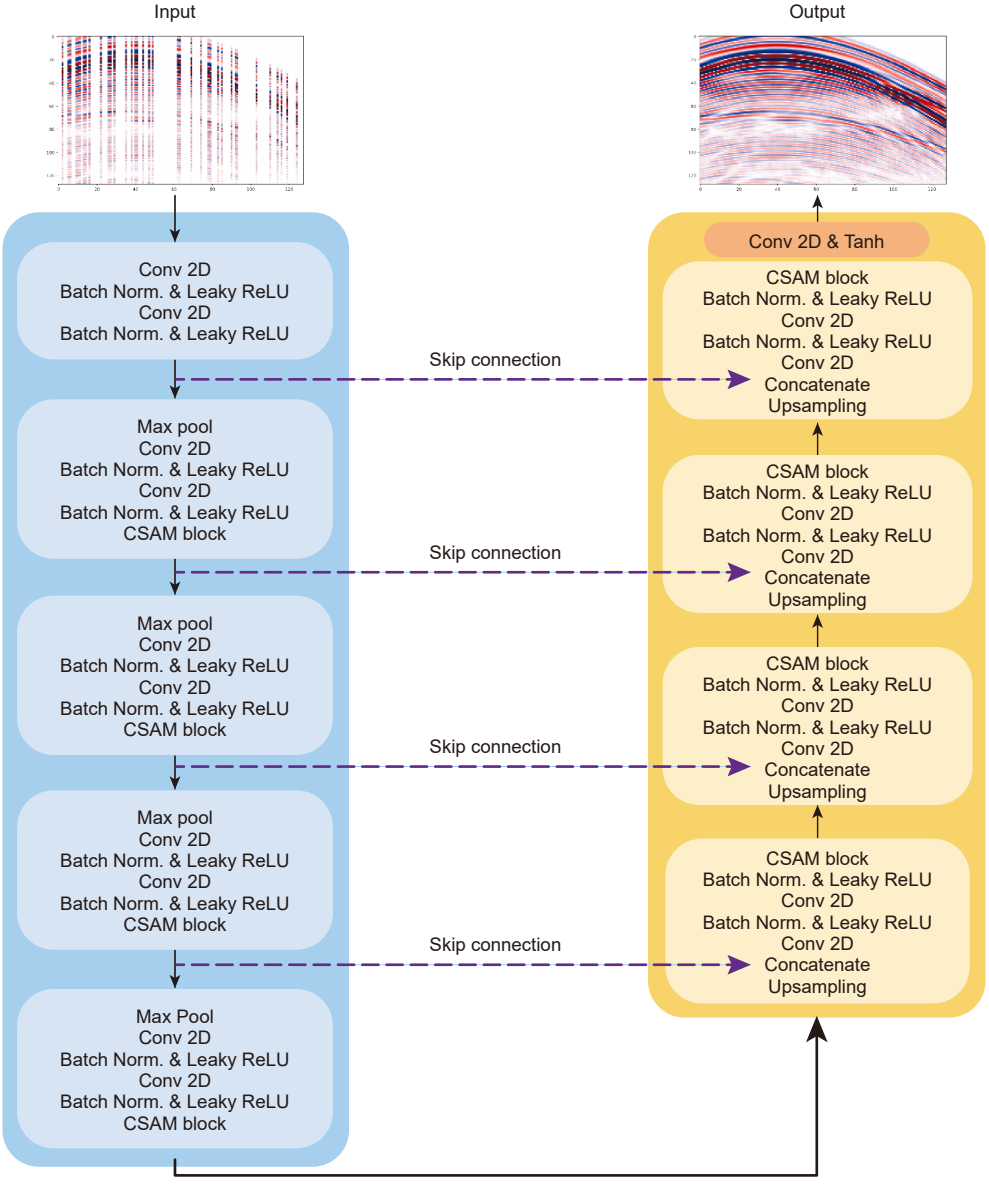

Fig. 4. The architecture of channel-spatial attention mechanism U-net.

layer, which restores the channel dimension to the original size C. The resulting feature is then reshaped back to its original dimensions $B \times C \times H \times W$ and normalized via a Sigmoid function to produce the channel attention map $A_c(Y_1)$.

2.1.2. Spatial attention submodule

The workflow of the spatial attention submodule is illustrated in Fig. 2(b). To focus on spatial information, convolutional layers are employed to integrate spatial features. The core of this submodule consists of two convolutional layers with a kernel size of 7×7 and a padding of 3. The input feature Y_2 is first passed through the initial convolutional layer, which reduces the channel dimension to C/r. This is followed by a batch normalization layer, producing a feature map with dimensions $B \times (C/r) \times H \times W$. Subsequently, the second convolutional layer restores the channel dimension to its original size C, followed by a second batch normalization layer, yielding a feature map of the original dimensions $B \times C \times H \times W$. Finally, the output is normalized using a Sigmoid function to generate the spatial attention map $A_s(Y_2)$.

2.2. U-net network overview

The U-net architecture in Fig. 3 was initially proposed for medical image segmentation (Rnneberger et al., 2015). Its core structure consists of a symmetric encoder-decoder framework, where skip connections are employed to integrate low level detail information from the encoder with high level semantic information from the decoder. This design effectively preserves both global semantics and local details within the features. During the encoding phase, the network extracts features through a series of convolutional layers and max-pooling operations. Convolutions capture spatial and contextual information, while max-pooling progressively reduces spatial resolution to enable hierarchical extraction of global features. As down-sampling progresses, the number of feature maps increases, enhancing the network's capacity to learn complex features. In the decoding phase, the network restores spatial resolution through up-sampling operations while leveraging skip connections to directly retrieve corresponding feature maps from the encoding phase. This facilitates the fusion of low-level details with high-level semantics. Ultimately, the decoder outputs feature maps with the same resolution as the original input image. A 1×1 convolutional layer is typically applied to adjust the number of feature channels to match the target classes, followed by a Softmax or Sigmoid activation function to perform classification or regression tasks. However, for the task of interpolating missing seismic data, the standard U-net structure has limitations, particularly in modeling long-range dependencies. This weakness can hinder the network's performance in complex scenarios where capturing global contextual information is crucial.

3. Network architecture

The primary objective of this study is to establish a mapping relationship between incomplete seismic data and complete seismic data to accomplish seismic data interpolation. To address the limited capability of the U-net architecture in modeling long-range dependencies, we adopt the U-net network as a backbone and design the CSAMUnet model in Fig. 4. The innovation of this model lies in the introduction of a channel-spatial attention mechanism module (depicted in Fig. 1) after two consecutive convolutional layers. This module aims to enhance global feature interactions and reduce information loss, thereby comprehensively improving the model's feature representation capability. For detailed operations and descriptions of the proposed model, refer to Table 1.

The CSAM block primarily consists of a channel attention submodule in Fig. 2(a) and a spatial attention submodule in Fig. 2(b). By constructing a global attention distribution, the block effectively captures long-range dependencies within the input feature map. Specifically, the channel attention submodule calculates channel attention weights, which are normalized using a sigmoid function. The input feature map Y_1 is then element-wise multiplied with $A_c(Y_1)$, resulting in the weighted feature map Y_2. This weighted feature map Y_2 serves as the input to the spatial attention submodule. The design of the channel attention submodule emphasizes preserving information. By focusing on the relative importance of different channels, this module optimizes the global feature distribution. The spatial attention submodule takes Y_2, the output of the channel attention submodule, as its input. It computes spatial attention weights, which are also normalized using a sigmoid function, producing $A_s(Y_2)$. The feature map Y_2 is then element-wise multiplied with $A_s(Y_2)$ to generate the final output feature map Y_3, which has the same dimensions as the input feature map Y_1. This design highlights significant regions in the spatial dimension, effectively enhancing local detail information. To avoid the potential loss of critical information caused by max-pooling operations, the module does not use max-pooling to retain as much feature information as possible, thereby minimizing information loss. The

Table 2
Comparison of parameters across different methods.

Model	Training time, h	Inference time, s	Parameter count, M	Memory footprint, MiB
U-net	5.42	0.1002	31.042369	3954
ECAUnet	5.98	0.1078	31.042396	4658
Proposed	10.94	0.2141	74.679489	9064

Table 1
The detailed operations of the proposed model.

Layer	Input size	Output size	Description
Input (x0)	(8, 1, 128, 128)	(8, 1, 128, 128)	Input data
In_conv (x1)	(8, 1, 128, 128)	(8, 64, 128, 128)	Double_conv (1 → 64)
Downsampling1 (x2)	(8,64, 128, 128)	(8, 128, 64, 64)	MaxPool2D + Double_conv + CSAM (64 → 128)
Downsampling2 (x3)	(8, 128, 64, 64)	(8, 256, 32, 32)	MaxPool2D + Double_conv + CSAM (128 → 256)
Downsampling3 (x4)	(8, 256, 32, 32)	(8, 512, 16, 16)	MaxPool2D + Double_conv + CSAM (256 → 512)
Downsampling4 (x5)	(8, 512, 16, 16)	(8, 1024, 8, 8)	MaxPool2D + Double_conv + CSAM (512 → 1024)
Upsampling1	(8, 1024, 8, 8) + x4	(8, 512, 16, 16)	ConvTranspose2D (1024 → 512) + Concat + Double_conv + CSAM (1024 → 512)
Upsampling2	(8, 512, 16, 16) + x3	(8, 256, 32, 32)	ConvTranspose2D (512 → 256) + Concat + Double_conv + CSAM (512 → 256)
Upsampling3	(8, 256, 32, 32) + x2	(8, 128, 64, 64)	ConvTranspose2D (256 → 128) + Concat + Double_conv + CSAM (256 → 128)
Upsampling4	(8, 128, 64, 64) + x1	(8, 64, 128,128)	ConvTranspose2D (128 → 64) + Concat + Double_conv + CSAM (128 → 64)
Output Conv	(8,64, 128,128)	(8, 1, 128, 128)	Conv2D (64 → 1) + tanh (Output data)

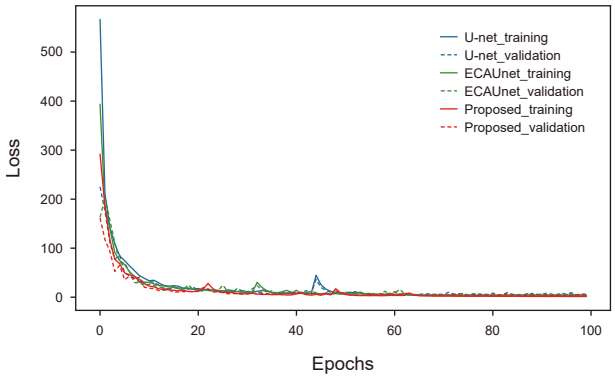

Fig. 5. Training and validation loss for three different methods.

integration of the two submodules not only enables the extraction of key features but also suppresses irrelevant or redundant information, preventing the network from being confined to a limited local receptive field, thus ensuring a balanced emphasis on both global context and local details and enhancing the overall feature representation capability.

The proposed network architecture in Fig. 4 is structured as follows: Encoding Stage (left side): Each layer in the encoding phase consists of convolution, batch normalization, a LeakyReLU activation function, a CSAM block, and a max-pooling layer. The number of convolutional kernels increases progressively as 64, 128, 256, 512, and 1024. This phase extracts hierarchical feature representations while gradually reducing spatial resolution. Decoding Stage (right side): Each layer in the decoding phase includes upsampling, convolution, batch normalization, a LeakyReLU activation, and a CSAM block. The number of convolutional filters mirrors the encoding phase in reverse order (1024, 512, 256, 128, 64). The final output matches the spatial dimensions of the original input image dimensions, ensuring consistent spatial resolution. The incorporation of the attention mechanism enables the proposed network to more precisely focus on critical regions, significantly enhancing its feature representation capability. This provides an efficient and reliable solution for seismic data interpolation and reconstruction tasks.

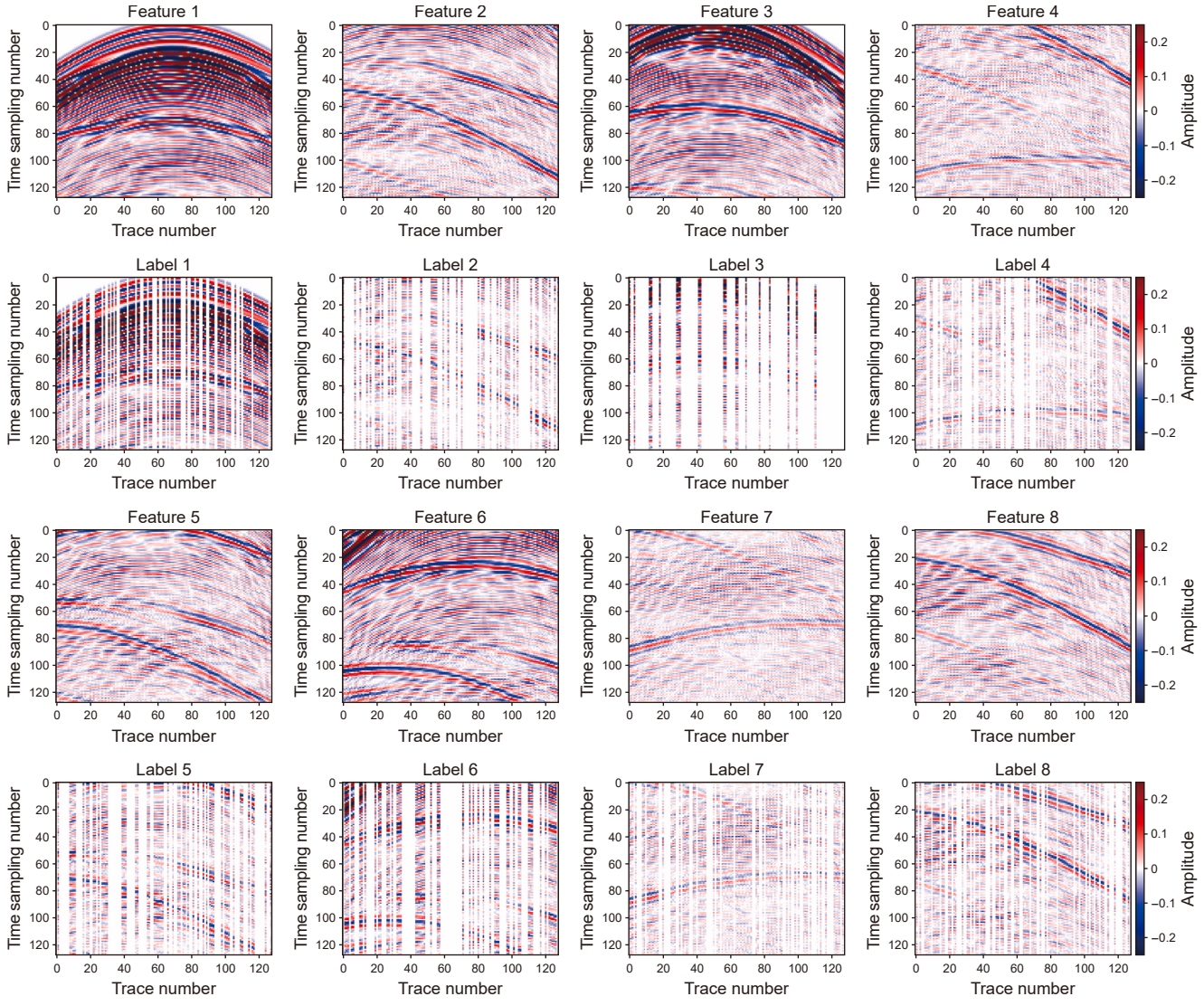

Fig. 6. Partial slice visualization of seismic reflection feature and label.

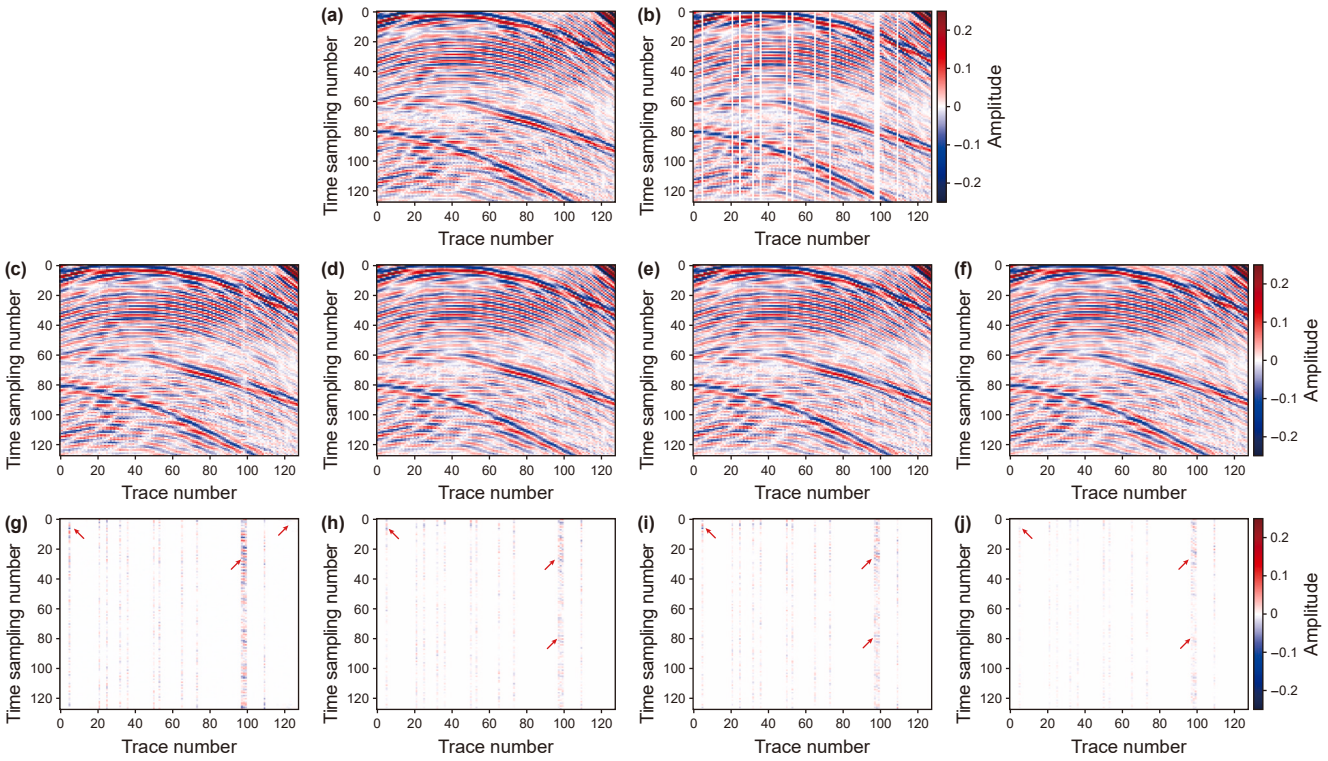

Fig. 7. Reconstruction results for 10.16% random trace missing. **(a)** shows the complete original data, **(b)** shows the randomly missing seismic data. **(c)**–**(f)** correspond to the reconstruction results of Fourierpocs, U-net, ECAUnet and the proposed method, respectively, and **(g)**–**(j)** depict the corresponding residual maps for each reconstruction result.

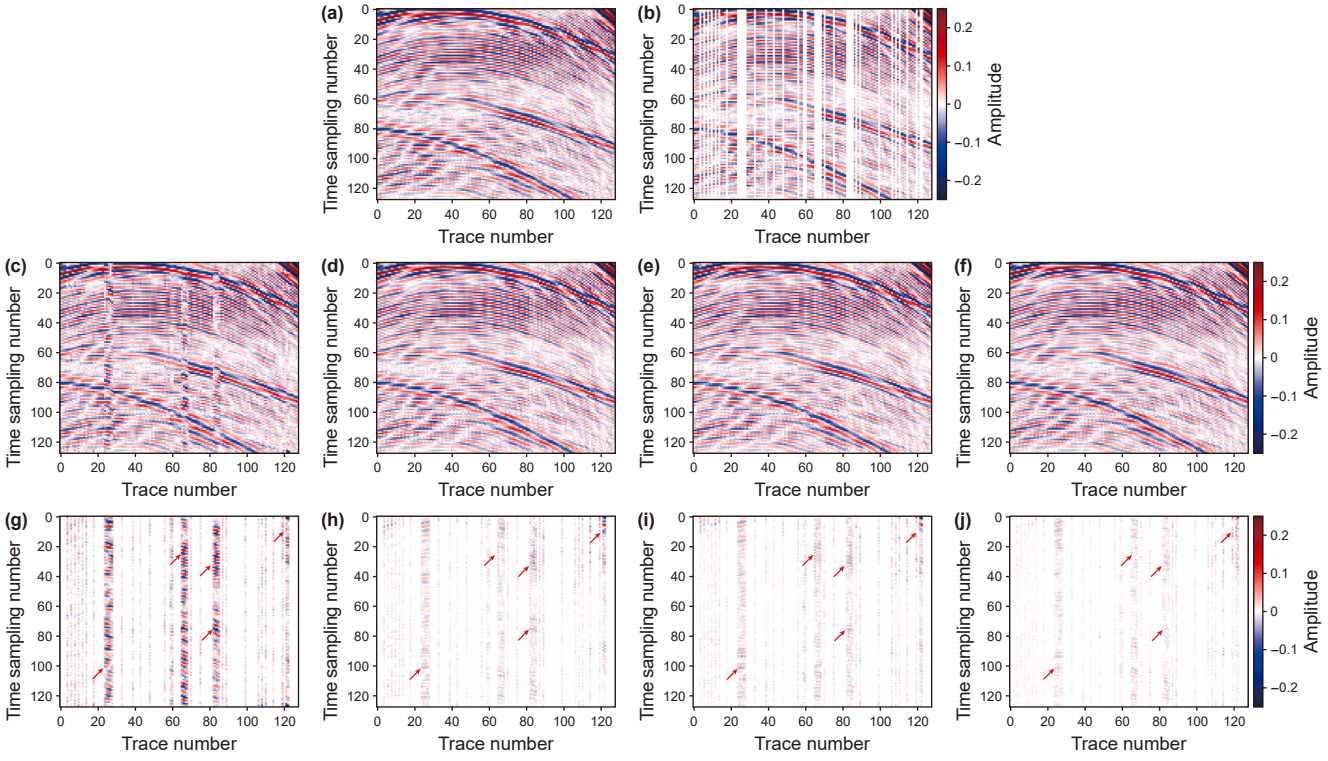

Fig. 8. Reconstruction results for 30.47% random trace missing. **(a)** shows the complete original data, **(b)** shows the randomly missing seismic data. **(c)**–**(f)** correspond to the reconstruction results of Fourierpocs, U-net, ECAUnet and the proposed method, respectively, and **(g)**–**(j)** depict the corresponding residual maps for each reconstruction result.

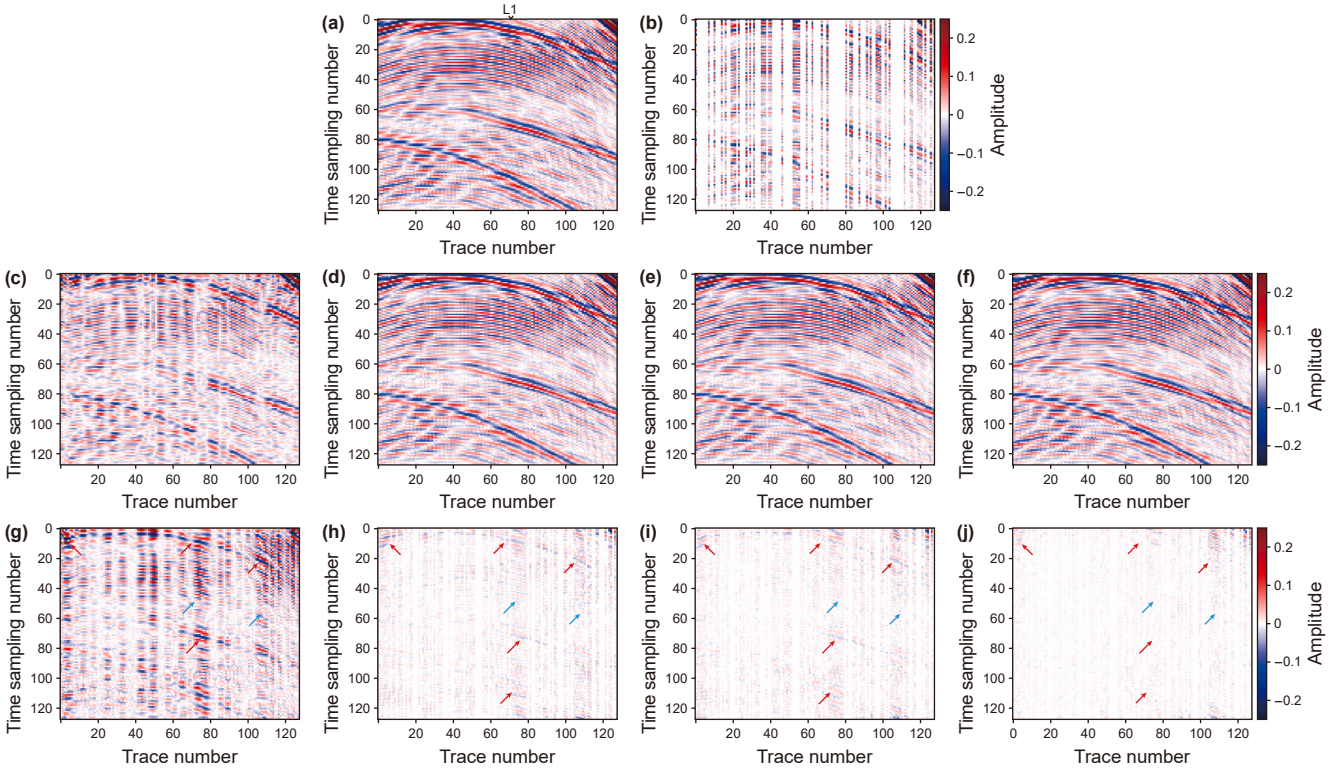

Fig. 9. Reconstruction results for 64.06% random trace missing. **(a)** shows the complete original data, **(b)** shows the randomly missing seismic data. **(c)**–**(f)** correspond to the reconstruction results of Fourierpocs, U-net, ECAUnet and the proposed method, respectively, and **(g)**–**(j)** depict the corresponding residual maps for each reconstruction result.

4. Experiments

4.1. Dataset and training

The experiments were conducted using the publicly available SEG C3 synthetic dataset and the Mobil AVO Viking Graben Line 12 real-world 2D marine seismic dataset. These datasets consist of 45 shot gathers, with a sampling rate of 8 ms. The SEG C3 dataset has a receiver grid resolution of 201 × 201. The Mobil AVO dataset has a temporal sampling interval of 4 ms and a spatial sampling interval of 25 m. To create the labeled data, the missing data ratio was randomly set between 30% and 80%. The data was filtered, normalized, and split into training, validation, and test sets in an 8:1:1 ratio. A small subset of the training data pairs is shown in Fig. 6. For information on training time, inference time, parameter count and memory footprint required by different network models, refer to Table 2. The training was conducted with a batch size of 8, learning rate of 1e−4, and the number of epochs was set to 100. We used the Adam optimizer, and the learning rate was automatically reduced to 10% of its original value if there is no improvement in the validation loss within every 10 epochs. This method helps the optimizer avoid getting stuck in local minima, maintains more stable learning during the training process, and also helps prevent overfitting. However, small fluctuations may occur when adjusting the learning rate, as shown by the red curve in Fig. 5, where slight fluctuations are observed at the 22nd, 49th, and 61st epochs when the learning rate is adjusted. The loss function, based on mean squared error (MSE), is defined in Eq. (3):

$$\mathrm{MSE} = \frac{1}{n}\sum_{i=1}^{n}(y_i - \hat{y}_i)^2 \tag{3}$$

where, n represents the number of samples in the dataset. y_i denotes the ground truth (or true value), and $\hat{y}_i$ represents the

Table 3
Interpolation results of different methods on synthetic test data samples with 10.16%, 20.31%, 30.47%, 40.62%, 50.78%, 64.06% and 75% randomly missing traces.

Methods	Metrics	10.16%	20.31%	30.47%	40.62%	50.78%	64.06%	75%
Fourierpocs	SNR	20.9878	13.5368	9.2245	4.0950	2.7090	1.9811	1.1584
	MAE	0.0014	0.0031	0.0076	0.0168	0.0214	0.0265	0.0308
	SSIM	0.9938	0.9836	0.9214	0.8049	0.7397	0.6408	0.5832
U-net	SNR	24.8522	18.1526	17.9808	13.7313	11.4392	15.6811	5.4448
	MAE	0.0008	0.0017	0.0027	0.0040	0.0060	0.0051	0.0168
	SSIM	0.9976	0.9948	0.9904	0.9883	0.9771	0.9848	0.8517
ECAUnet	SNR	24.8286	18.3584	18.1665	14.2874	11.4083	16.7475	5.7456
	MAE	0.0008	0.0017	0.0027	0.0039	0.0060	0.0044	0.0161
	SSIM	0.9976	0.9946	0.9900	0.9879	0.9773	0.9878	0.8591
Proposed	SNR	27.7980	21.4370	21.0988	15.9728	13.8313	**20.0793**	6.9853
	MAE	0.0005	0.0012	0.0019	0.0029	0.0045	**0.0029**	0.0129
	SSIM	0.9987	0.9975	0.9948	0.9931	0.9852	**0.9939**	0.9028

Bold indicates the best result for each metric on randomly missing 64.06% traces.

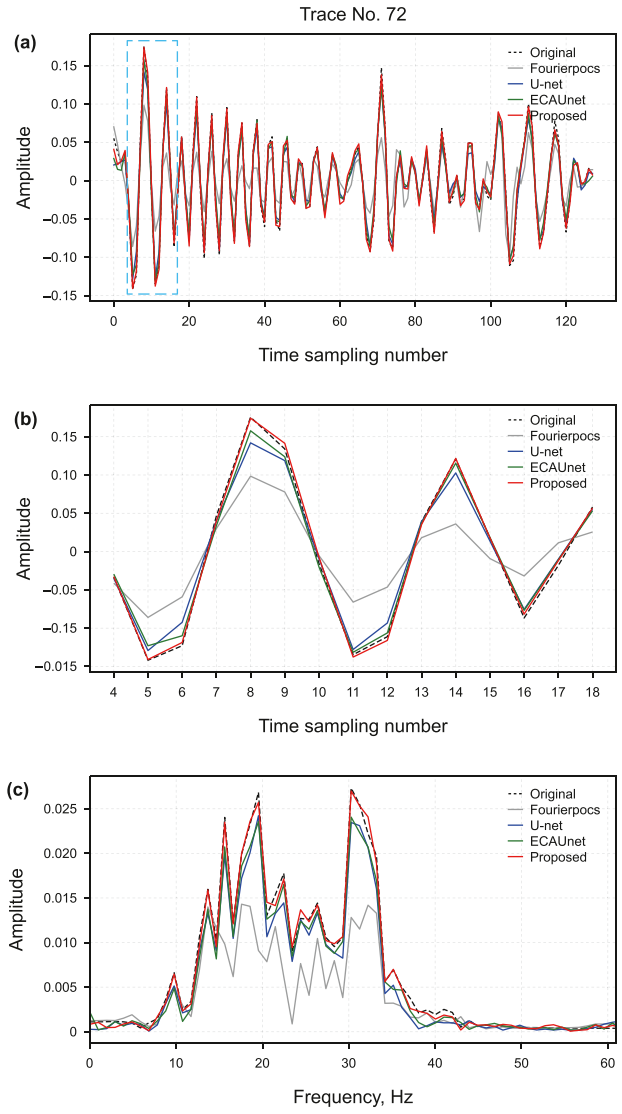

Fig. 10. **(a)** Single trace seismic data reconstruction results location L_1 (Fig. 9(a)) using different methods, **(b)** local magnification of the blue-boxed reconstruction results, **(c)** spectrum comparison of single trace seismic data reconstruction.

predicted value from the model. The term $(y_i - \hat{y}_i)^2$ calculates the squared difference between the predicted value and the ground truth for each sample.

4.2. Evaluation metrics

This study employs the signal to noise ratio (SNR), mean absolute error (MAE), and structural similarity index measure (SSIM) (Wang et al., 2004) to evaluate the quality of the reconstructed seismic data. The equations are as follows:

$$\mathrm{SNR} = 10\log_{10}\left(\frac{\|y_i\|_2^2}{\|y_i - \hat{y}_i\|_2^2}\right) \tag{4}$$

$$\mathrm{MAE} = \frac{1}{n}\sum_{i=1}^{n}|\hat{y}_i - y_i| \tag{5}$$

The final SSIM value is obtained by averaging the SSIM map, which quantifies the spatial distribution of differences between two datasets. While the visualization of the SSIM map provides a clear depiction of the spatial distribution of reconstruction differences. In this study, Eqs. (4)–(6) are used to quantify the experimental results.

$$\mathrm{SSIM}(y_i, \hat{y}_i) = \frac{\left(2\mu_{y_i}\mu_{\hat{y}_i} + C_1\right)\left(2\sigma_{y_i}\sigma_{\hat{y}_i} + C_2\right)}{\left(\mu_{y_i}^2 + \mu_{\hat{y}_i}^2 + C_1\right)\left(\sigma_{y_i}^2 + \sigma_{\hat{y}_i}^2 + C_2\right)} \tag{6}$$

where, y_i is the true seismic data, $\hat{y}_i$ is after interpolation seismic data, μ_{y_i} is the mean of y_i, $\mu_{\hat{y}_i}$ is the mean of $\hat{y}_i$, $\sigma_{y_i}^2$ is the variance of y_i, $\sigma_{\hat{y}_i}^2$ is the variance of $\hat{y}_i$, $\sigma_{y_i}\sigma_{\hat{y}_i}$ is the covariance of y_i and $\hat{y}_i$, C_1 and C_2 used to stabilize the calculation and prevent the denominator from being zero.

4.3. Test on synthetic data

4.3.1. Sparsity sensitivity analysis

The testing results of synthetic data slices with three different missing proportions are first presented (Figs. 7–9), with quantitative evaluation metrics shown in Table 3. With 10.16% random trace missing (Fig. 7(b)), all four methods can generally complete missing trace reconstruction, with subtle differences mainly observed in the recovery of strong reflection events, as indicated by red arrows in Fig. 7(g)–(j). For 30.47% random trace missing (Fig. 8(b)), the reconstruction results (Fig. 8(c)–(f)) demonstrate varying performance in amplitude recovery: Fourierpocs (Fig. 8(c)) achieves basic reconstruction but with low accuracy, evident from white vertical bars, while U-net (Fig. 8(d)) and ECAUnet (Fig. 8(e)) show improvements yet still underperform at strong reflection events. In contrast, the proposed method (Fig. 8(f)) exhibits superior accuracy and continuity in recovering high-energy reflection amplitudes, as evidenced by red arrows in Fig. 8(g)–(j). When trace missing increases to 64.06% (Fig. 9(b)), exceeding 50% missing data severely limits Fourierpocs's performance (Fig. 9(c)) due to insufficient effective information. Although U-net (Fig. 9(d)) and ECAUnet (Fig. 9(e)) show noticeable improvements, they still struggle in regions with extensive trace missing. The proposed method (Fig. 9(f)) demonstrates remarkable precision and continuity even in heavily missing areas, with gradually weakening reflection contours and residual energy clearly observable at red

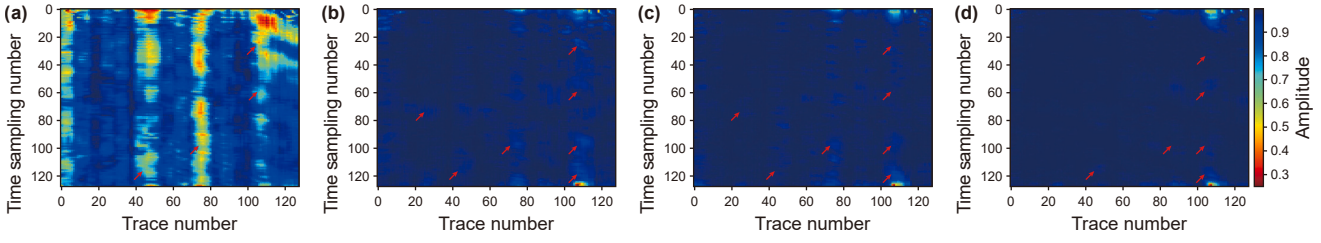

Fig. 11. Structural similarity index measure (SSIM) visualization results on synthetic data. **(a)–(d)** Reconstruction results of Fourierpocs, U-net, ECAUnet and the proposed method.

and blue arrow locations in Fig. 9(g)–(j), a trend further confirmed by SSIM visualization in Fig. 11. We can clearly observe that the proposed method achieves the highest structural similarity.

Single trace analysis of reconstruction results (Fig. 10) provides detailed validation, The amplitude reconstruction (Fig. 10(a)) and its zoomed view (Fig. 10(b)) reveal that Fourierpocs (gray line) recovers basic waveform but lacks amplitude accuracy, U-net (blue line) shows significant deviation at abrupt amplitude changes, and ECAUnet (green line) improves upon U-net but still exhibits local peak-and-trough errors. The proposed method (red line) optimally reconstructs complex details including abrupt amplitude variations, achieving the highest waveform fidelity. The frequency spectrum (Fig. 10(c)) confirms the proposed method's superior amplitude preservation, particularly in mid frequency bands where other methods show varying degrees of amplitude loss. Full shot gather reconstruction results are displayed in Fig. 12, with interpolation outputs (Fig. 12(b)–(e)) and corresponding residual maps (Fig. 12(g)–(j)). Blue and red arrows highlight reflection events where contour sharpness and residual energy display progressive improvement. Comprehensive evaluation through reconstruction quality, residual maps, quantitative metrics, SSIM visualization, and single-trace analysis demonstrates the proposed method's enhanced capability in capturing complex wavefield features and preserving seismic amplitude characteristics, enabling accurate restoration of missing trace amplitudes.

4.3.2. Noise sensitivity analysis

To further test the model's performance under different noise levels, we conducted a noise sensitivity test (Table 4) and showed the interpolation results with corresponding residual maps under light, moderate and severe noise conditions in Fig. 13. Under light noise (Fig. 13(a)), the interpolation results (Fig. 13(a1)–(a3)) show generally good recovery of missing traces. Detailed examination of the residual maps (Fig. 13(a4)–(a6), indicated by red arrows) reveal that while both U-net and ECAUnet retain residual contours of strong reflection events, the proposed method shows virtually no such artifacts and maintains significantly lower residual energy even with extensive trace loss. For moderate noise (Fig. 13(b)), the interpolation results (Fig. 13(b1)–(b3)) demonstrate adequate trace recovery, though residual maps (Fig. 13(b4)–(b6)) show that weak reflection events are partially submerged by noise, notably, strong reflection events still exhibit residual contours in U-net and ECAUnet results but are effectively eliminated by the proposed method. Under severe noise (Fig. 13(c)), the interpolation results (Fig. 13(c1)–(c3)) indicate that strong reflection events become distorted while weak reflections are completely covered, with residual maps (Fig. 13(c4)–(c6)) dominated by noise. Overall, the proposed model successfully interpolates missing traces under light-to-moderate noise conditions, though its performance degrades under severe noise where it can only recover strong reflection events while failing to reconstruct weaker ones due to noise interference.

Table 4
Sensitivity testing of the model on synthetic data with input signal-to-noise ratio (SNR) ranging from 5 dB to 25 dB.

Model	Metrics	5 dB	10 dB	15 dB	20 dB	25 dB
U-net	SNR	6.6998	10.0454	12.7898	14.4190	15.0652
	MAE	0.0218	0.0137	0.0092	0.0068	0.0055
	SSIM	0.7681	0.9026	0.9584	0.9772	0.9836
ECAUnet	SNR	6.5999	10.0681	12.9264	14.8054	15.5071
	MAE	0.0219	0.0137	0.0092	0.0066	0.0053
	SSIM	0.7631	0.9023	0.9578	0.9778	0.9844
Proposed	SNR	7.0246	10.7760	14.1230	16.4298	17.4726
	MAE	0.0215	0.0130	0.0084	0.0058	0.0045
	SSIM	0.7701	0.9084	0.9636	0.9829	0.9892

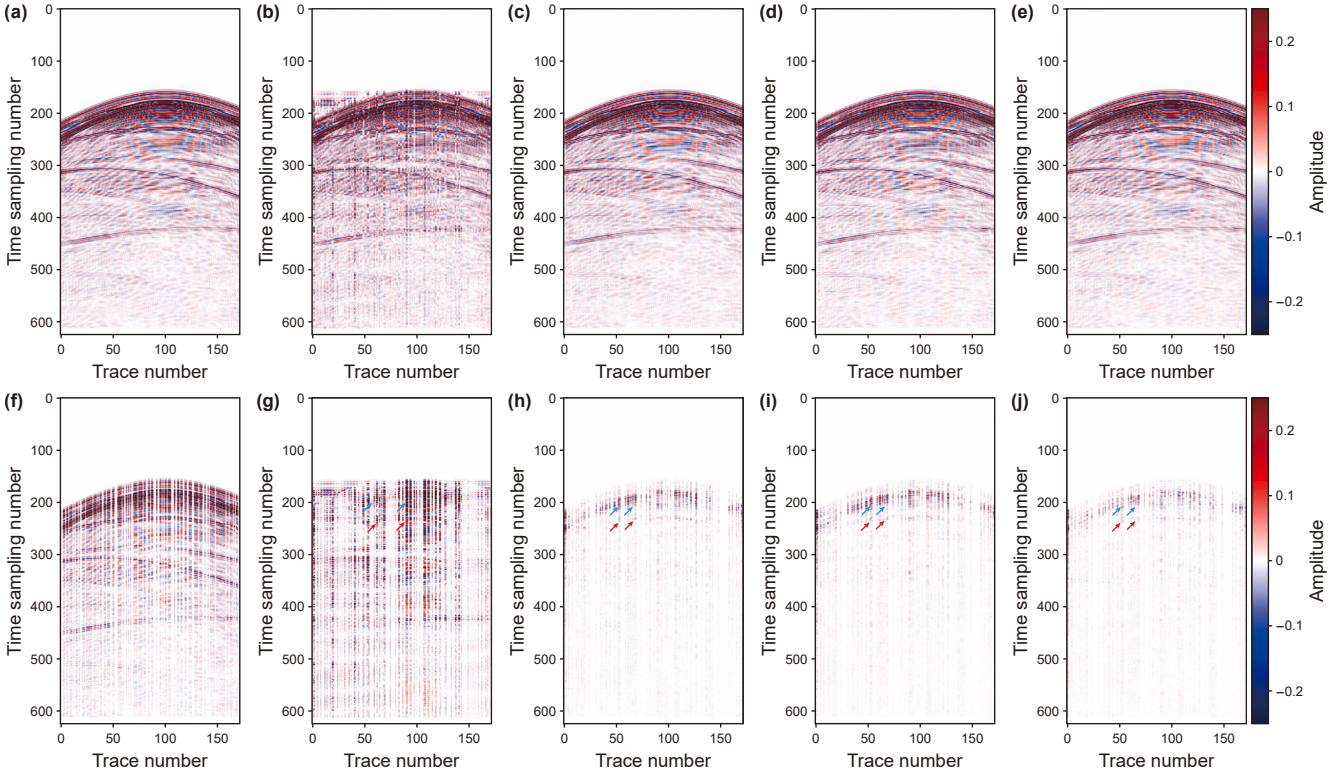

Fig. 12. The comparison of synthetic data results. **(a)** shows the complete data. **(f)** shows the randomly missing data. **(b)–(e)** correspond to the reconstruction results of Fourierpocs, U-net, ECAUnet and the proposed method, respectively, and **(g)–(j)** depict the corresponding residual maps for each reconstruction result.

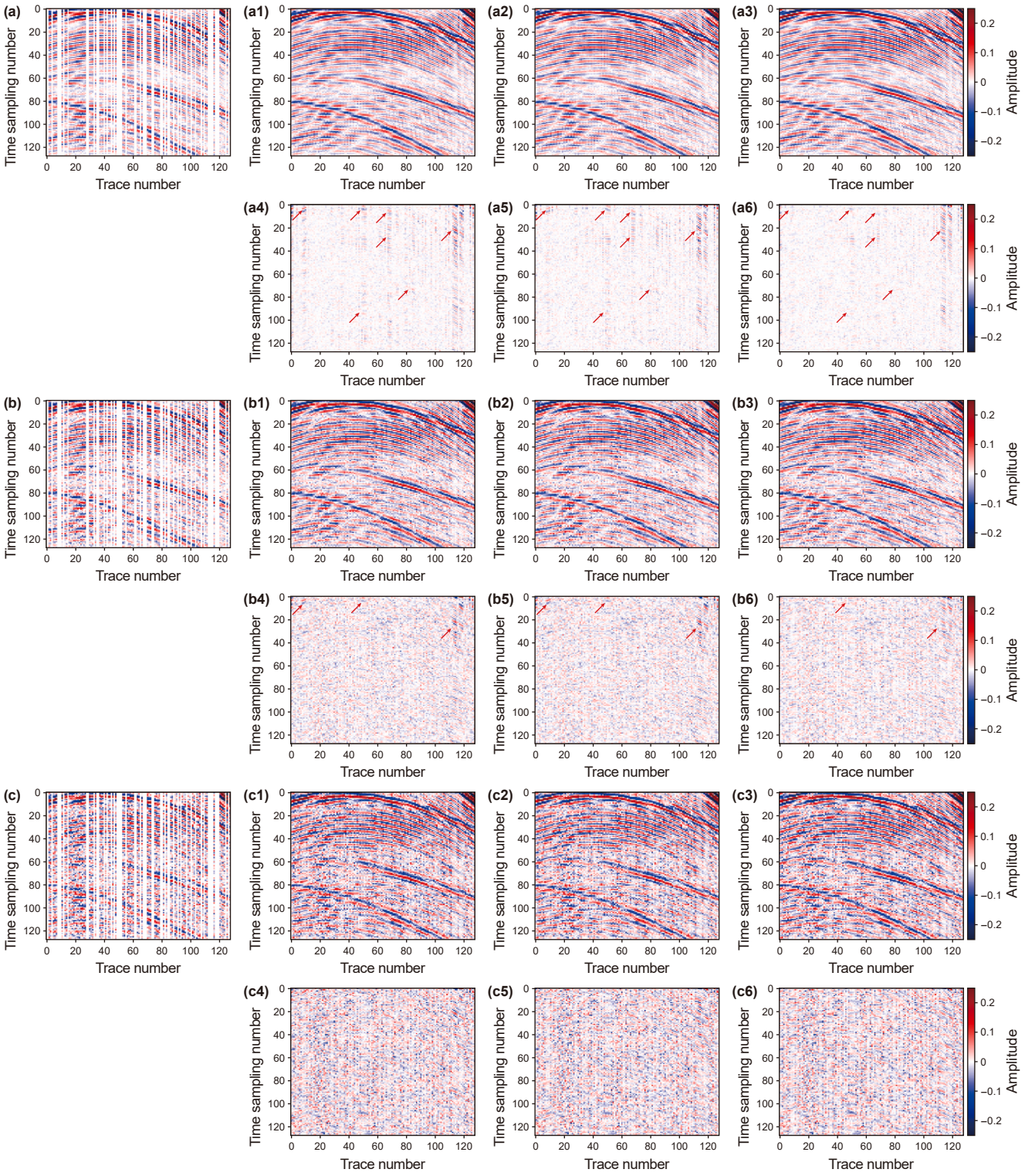

Fig. 13. Noise sensitivity test. Subfigures **(a)**, **(b)**, **(c)** show the input data with mild, moderate, and severe noise added, respectively. For each noise level, the interpolation results from U-net, ECAUnet, and the proposed method are presented in the first row (e.g., **(a1)**–**(a3)**, **(b1)**–**(b3)**, **(c1)**–**(c3)**), with the corresponding residual maps displayed in the second row (e.g., **(a4)**–**(a6)**, **(b4)**–**(b6)**, **(c4)**–**(c6)**).

4.4. Test on field data

To validate the effectiveness of the proposed method, the Mobil AVO Viking Graben Line 12 publicly available 2D marine seismic dataset was used for testing. The temporal and spatial sampling intervals are 4 ms and 25 m, respectively. From this dataset, 40 shot gathers were selected and sliced into patches of size 120 × 120. Two shot gathers were reserved for testing, while the remaining slices were used for training and validation. Using a scenario with 30% randomly missing traces as an example,

Fig. 14(f)–(h) display the residual maps. In addition, by analyzing the SSIM visualizations in Fig. 15 and quantitative analysis in Table 5, the regions indicated by red arrows in Fig. 15(a)–(d) reveal that the proposed method achieves higher similarity between the interpolated data and the ground truth. This indicates that the input feature maps processed by the network, which incorporates channel-spatial attention mechanisms, establishing an effective connection between local reflection characteristics and global geological structures. Consequently, the proposed method demonstrates superior performance in reconstructing randomly missing trace information. Meanwhile, we applied the proposed method to actual oilfield data from Jiangsu Oilfield. We present the results for one shot record as an example. As shown in Fig. 16(a), the original data exhibits poor quality with severe noise interference. Fig. 16(b) shows the randomly missing data. Fig. 16(c)–(f) present the reconstruction results from Fourierpocs, U-net, ECAUnet and the proposed method, while Fig. 16(g)–(j) display their corresponding residual maps. Combined with quantitative analysis (Table 6), the proposed method demonstrates superior performance in the interpolation task.

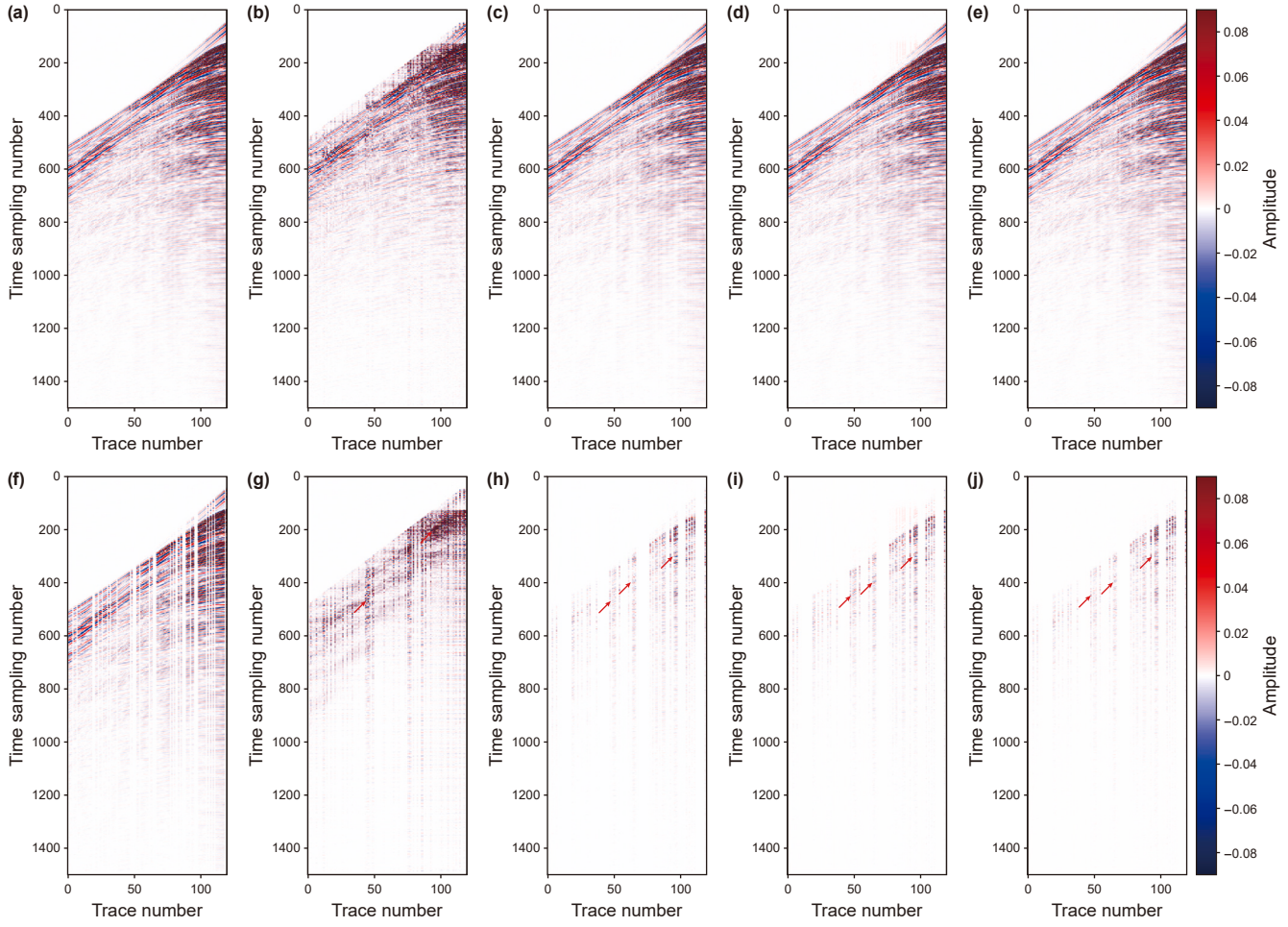

Fig. 14. Reconstruction results on marine seismic data. **(a)** shows the complete data. **(f)** shows the randomly missing data. **(b)–(e)** display the reconstruction results of Fourierpocs, U-net, ECAUnet and the proposed method, respectively. **(g)–(j)** depict the corresponding residual maps for each reconstruction result.

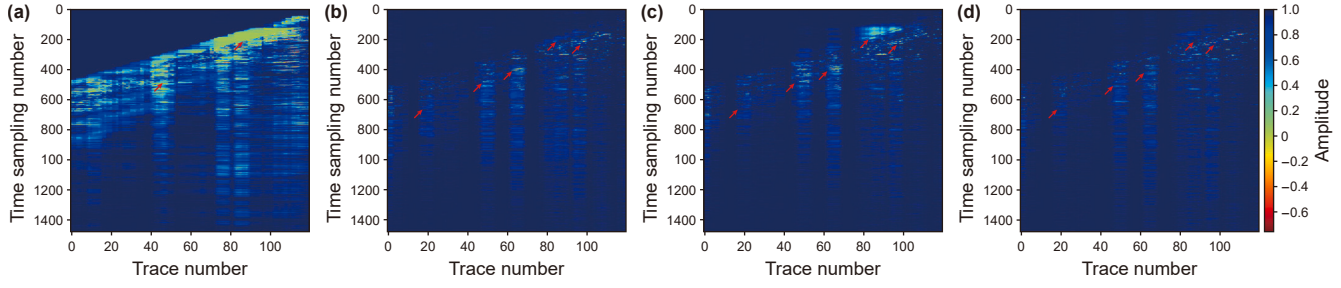

Fig. 15. Structural similarity index measure (SSIM) visualization results on marine data. **(a)–(d)** reconstruction results of Fourierpocs, U-net, ECAUnet and the proposed method.

Table 5
Interpolation results of different methods on marine data.

Methods	SNR	MAE	SSIM
Fourierpocs	11.2047	0.0173	0.8894
U-net	20.5377	0.0027	0.9893
ECAUnet	20.4159	0.0026	0.9899
Proposed	21.3223	0.0015	0.9983

Table 6
Interpolation results of different methods on field data from Jiangsu Oilfield.

Methods	SNR	MAE	SSIM
Fourierpocs	2.5930	0.0149	0.8034
U-net	9.8745	0.0032	0.9793
ECAUnet	10.4985	0.0028	0.9831
Proposed	11.9734	0.0017	0.9904

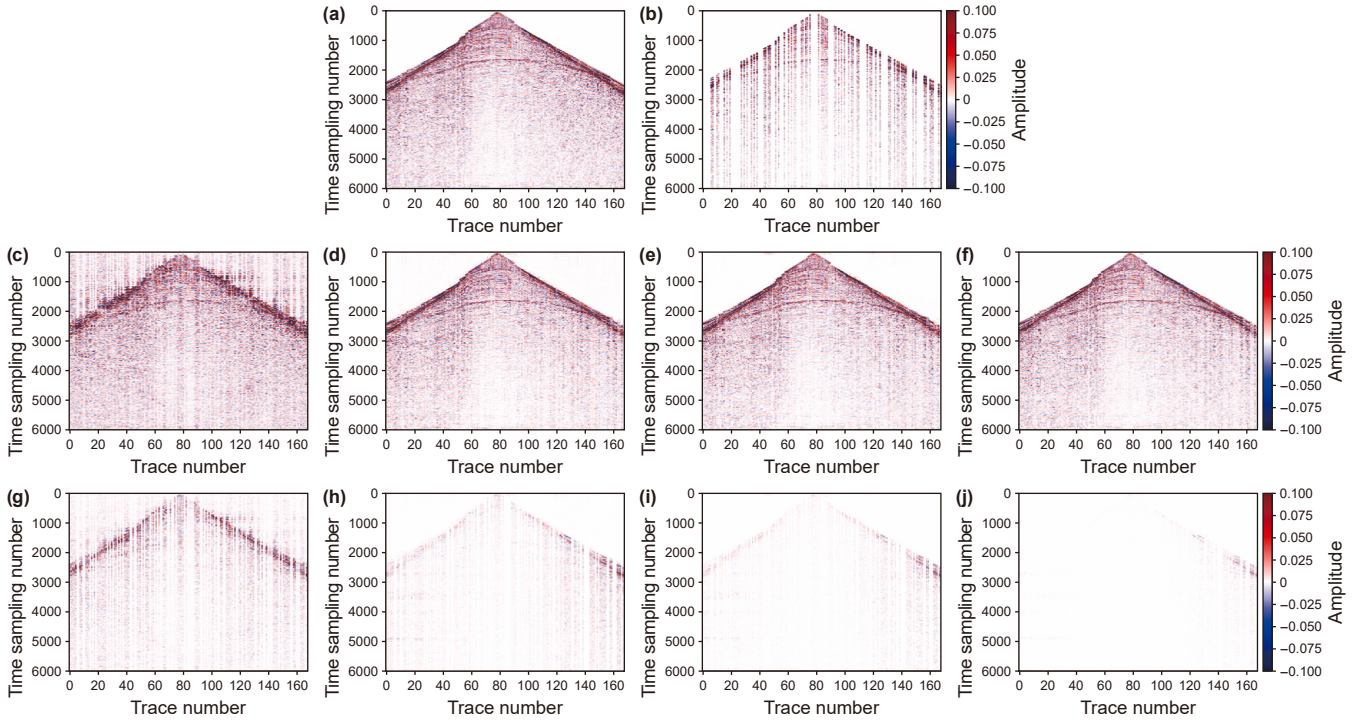

Fig. 16. Reconstruction results on field data from Jiangsu Oilfield. **(a)** shows the complete data. **(b)** shows the randomly missing data. **(c)–(f)** display the reconstruction results of Fourierpocs, U-net, ECAUnet and the proposed method, respectively. **(g)–(j)** depict the corresponding residual maps for each reconstruction result.

5. Conclusion

This study focused on the interpolation of field-acquired seismic data and proposed a solution based on deep learning with dual channel-spatial attention mechanism to successfully accomplishing the interpolation task. By introducing a dual channel-spatial attention mechanism module (CSAM), the reconstruction capability of the network for missing seismic data has been significantly improved. Specifically, the channel attention submodule models global contextual information along the channel dimension of the feature map and dynamically generates channel weight distributions. The spatial attention submodule focuses on saliency information in the spatial dimension of the feature map, extracting saliency distributions at each pixel position. The synergistic mechanism of these two modules strengthens the connection between local reflection features and global feature structures, thereby enhancing feature representation. Finally, through sparsity sensitivity tests and noise sensitivity tests on synthetic data, as well as field data validation, combined with evaluation metrics including SNR, MAE, and SSIM, the proposed method demonstrates superiority in reconstructing seismic reflection events and preserving amplitude fidelity for randomly missing seismic data, particularly in regions with extensive data missing.

6. Discussion

This work proposes a deep learning-based seismic data interpolation method with attention mechanisms, achieving high-precision reconstruction of randomly missing seismic traces through a supervised learning framework. The method exhibits three key advantages: First, by integrating the powerful feature extraction capability of convolutional neural networks with the global feature focusing properties of attention mechanisms, it effectively identifies critical reflection events in seismic data. Second, once trained, the model demonstrates exceptional inference efficiency, requiring only approximately 0.2 s per data sample. Third, the incorporated attention module enables adaptive feature weighting, significantly enhancing robustness in complex reflection zones. However, two limitations persist: (1) The method demands extensive training datasets, making the data preparation phase time-consuming. (2) Performance degrades noticeably when handling extreme missing scenarios (random trace loss exceeding 75%). To address these constraints by leveraging complementary training paradigms (e.g., unsupervised/self-supervised learning), future research will pursue two optimization directions: First, developing a self-supervised pretraining framework based on masked autoencoders, where tasks like random trace masking automatically generate pseudo-labels to reduce dependency on

manual annotations. Second, constructing a 3D Swin-Transformer architecture that exploits attention mechanisms across inline, crossline, and time dimensions to fully capture spatial continuity features in 3D seismic volumes.

CRediT authorship contribution statement

Chao Ma: Writing – review & editing, Writing – original draft, Visualization, Validation. **Jian-Ping Huang:** Supervision, Resources, Project administration, Funding acquisition. **Zi-Xuan Qiao:** Writing – review & editing. **San-Fu Li:** Writing – review & editing. **Wen-Sheng Duan:** Writing – review & editing. **Gang-Lin Lei:** Writing – review & editing.

Declaration of competing interests

The authors declare that they have no known competing financial interests or personal relationships that could have appeared to influence the work reported in this paper.

Acknowledgments

We thank four anonymous reviewers and editor Meng-Jiao Zhou for their comments that helped us to improve the manuscript. This study is supported by the National Natural Science Foundation of China (Grant No. 42374164), the High Precision Imaging Study of Small-scale and High-angle Structures in the Western Ordos Basin (Grant No. 2024D2ZZ01), the Imaging Study of Q Least Squares Migration (Grant No. 671024115010), the Research on Image Deconvolution Technology Based on Regularization (Grant No. 202418018212), the Research on the masked autoencoder method based on vit Network (Grant No. 30200020-24-ZC0613-0044) and the Taishan Scholars Research Program of Shandong Province.

References

Adamo, A., Mazzucchelli, P., Bienati, N., 2015. Irregular interpolation of seismic data through low-rank tensor approximation. In: 2015 IEEE International Geoscience and Remote Sensing Symposium (IGARSS), pp. 4292–4295. https://doi.org/10.1109/IGARSS.2015.7326775.

Bahdanau, D., Cho, K., Bengio, Y., 2014. Neural machine translation by jointly learning to align and translate. arXiv. https://doi.org/10.48550/arXiv.1409.0473.

Brandolin, F., Ravasi, M., Alkhalifah, T., 2024. Pinnslope: Seismic data interpolation and local slope estimation with physics informed neural networks. Geophysics 89 (4), V331–V345. https://doi.org/10.1190/geo2023-0323.1.

Chai, X., Gu, H., Li, F., Duan, H., Hu, X., Lin, K., 2020. Deep learning for irregularly and regularly missing data reconstruction. Sci. Rep. 10, 3302. https://doi.org/10.1038/s41598-020-59801-x.

Cheng, M., Lin, J., Lu, S., Dong, S., Dong, X., 2023. Seismic data reconstruction based on multiscale attention deep learning. IEEE Trans. Geosci. Rem. Sens. 61, 5914718. https://doi.org/10.1109/TGRS.2023.3298431.

Dou, Y., Li, K., Duan, H., Li, T., Dong, L., Huang, Z., 2023. MDA GAN: Adversarial-learning-based 3-D seismic data interpolation and reconstruction for complex missing. IEEE Trans. Geosci. Rem. Sens. 61, 5905014. https://doi.org/10.1109/TGRS.2023.3249476.

Fomel, S., 2003. Seismic reflection data interpolation with differential offset and shot continuation. Geophysics 68 (2), 733–744. https://doi.org/10.1190/1.1567243.

Gan, S., Wang, S., Chen, Y., Zhang, Y., Jin, Z., 2015. Dealiased seismic data interpolation using seislet transform with low-frequency constraint. IEEE Geosci. Rem. Sen. Letters 12, 2150–2154. https://doi.org/10.1109/lgrs.2015.2453119.

Guo, Y., Fu, L., Li, H., 2023. Seismic data interpolation based on multi-scale transformer. IEEE Geosci. Rem. Sensing Letters 20, 7504205. https://doi.org/10.1109/lgrs.2023.3298101.

He, T., Wu, B., Zhu, X., 2021. Seismic data consecutively missing trace interpolation based on multistage neural network training process. IEEE Geosci. Rem. Sen. Letters 19, 7504105. https://doi.org/10.1109/lgrs.2021.3089585.

Herrmann, F.J., Hennenfent, G., 2008. Non-parametric seismic data recovery with curvelet frames. Geophys. J. Int. 173, 233–248. https://doi.org/10.1111/j.1365-246x.2007.03698.x.

Huang, J., Chen, L., Wang, Z., Song, C., Han, J., 2023. Adaptive variable-grid least-squares reverse-time migration. Front. Earth Sci. 10, 1044072. https://doi.org/10.3389/feart.2022.1044072.

Jaderberg, M., Simonyan, K., Zisserman, A., et al., 2015. Spatial Transformer Networks. arXiv preprint, arXiv:1506.02025. https://doi.org/10.48550/arXiv.1506.02025.

Jia, Y., Ma, J., 2017. What can machine learning do for seismic data processing? An interpolation application. Geophysics 82 (3), V163–V177. https://doi.org/10.1190/geo2016-0300.1.

Li, X., Wu, B., Zhu, X., Yang, H., 2021. Consecutively missing seismic data interpolation based on coordinate attention unet. IEEE Geosci. Rem. Sen. letters 19, 1–5. https://doi.org/10.1109/lgrs.2021.3128511.

Li, Y., Alkhalifah, T., 2022. Target-oriented time-lapse elastic full-waveform inversion constrained by deep learning-based prior model. IEEE Trans. Geosci. Rem. Sens. 60, 4510812. https://doi.org/10.1109/tgrs.2022.3186028.

Li, Y., Zhang, H., Huang, J., Li, Z., 2024. Conditional denoising diffusion probabilistic model for ground-roll attenuation. IEEE Trans. Geosci. Rem. Sens. 62, 1–12. https://doi.org/10.1109/tgrs.2024.3489716.

Liu, Q., Fu, L., Zhang, M., 2021. Deep-seismic-prior-based reconstruction of seismic data using convolutional neural networks. Geophysics 86 (2), V131–V142. https://doi.org/10.1190/geo2019-0570.1.

Luo, Y., Zhang, G., Duan, J., Li, X., Liang, C., Zhong, Q., Ran, S., Cao, C., 2024. Multitask two-stage deep learning seismic strong and weak reflection separation. IEEE Trans. Geosci. Rem. Sens. 63, 5902311. https://doi.org/10.1109/tgrs.2024.3522989.

Luo, Y., Zhang, G., Liu, W., Zhang, J., Li, L., Li, X., Duan, J., 2023. Strata boundary-constrained multitask multihorizon tracking. IEEE Geosci. Rem. Sens. Letters 21, 7500405. https://doi.org/10.1109/lgrs.2023.3334215.

Ma, J., 2010. Improved iterative curvelet thresholding for compressed sensing and measurement. IEEE Trans. Instrum. Meas. 60, 126–136. https://doi.org/10.1109/tim.2010.2049221.

Ma, J., 2013. Three-dimensional irregular seismic data reconstruction via low-rank matrix completion. Geophysics 78 (5), V181–V192. https://doi.org/10.1190/geo2012-0465.1.

Ma, J., Plonka, G., 2010. The curvelet transform. IEEE Signal Process. Mag. 27, 118–133. https://doi.org/10.1109/MSP.2009.935453.

Mnih, V., Heess, N., Graves, A., Kavukcuoglu, K., 2014. Recurrent models of visual attention. Adv. Neural Inf. Process. Syst. 27. https://doi.org/10.48550/arXiv.1406.6247.

Naghizadeh, M., 2012. Seismic data interpolation and denoising in the frequency-wavenumber domain. Geophysics 77 (2), V71–V80. https://doi.org/10.1190/geo2011-0172.1.

Naghizadeh, M., Sacchi, M.D., 2007. Multistep autoregressive reconstruction of seismic records. Geophysics 72 (6), V111–V118. https://doi.org/10.1190/1.2771685.

Niu, X., Fu, L., Zhang, W., Li, Y., 2021. Seismic data interpolation based on simultaneously sparse and low-rank matrix recovery. IEEE Trans. Geosci. Rem. Sens. 60, 9100613. https://doi.org/10.1109/tgrs.2021.3110600.

Oropeza, V., Sacchi, M., 2011. Simultaneous seismic data denoising and reconstruction via multichannel singular spectrum analysis. Geophysics 76 (3), V25–V32. https://doi.org/10.1190/1.3552706.

Porsani, M.J., 1999. Seismic trace interpolation using half-step prediction filters. Geophysics 64 (5), 1461–1467. https://doi.org/10.1190/1.1444650.

Rnneberger, O., Fischer, P., Brox, T., 2015. U-net: convolutional networks for biomedical image segmentation. In: Medical Image Computing and computer-assisted intervention–MICCAI 2015: 18th International Conference, pp. 234–241. https://doi.org/10.48550/arXiv.1505.04597.

Ronen, J., 1987. Wave-equation trace interpolation. Geophysics 52 (7), 973–984. https://doi.org/10.1190/1.1442366.

Shan, W., Wang, Y., Lu, W., 2021. ECA-Unet: Denoise seismic data by learning from traditional method. In: SEG International Exposition and Annual Meeting, pp. 2904–2908. https://doi.org/10.1190/segam2021-3583394.1.

Siahsar, M.A.N., Gholtashi, S., Torshizi, E.O., Chen, W., Chen, Y., 2017. Simultaneous denoising and interpolation of 3-D seismic data via damped data-driven optimal singular value shrinkage. IEEE Geoscience and Geosci. Rem. Sens. Letters 14, 1086–1090. https://doi.org/10.1109/lgrs.2017.2697942.

Spitz, S., 1991. Seismic trace interpolation in the f-x domain. Geophysics 56 (6), 785–794. https://doi.org/10.1190/1.1443096.

Stolt, R.H., 2002. Seismic data mapping and reconstruction. Geophysics 67 (3), 890–908. https://doi.org/10.1190/1.1484532.

Sun, J., Slang, S., Elboth, T., Larsen Greiner, T., McDonald, S., Gelius, L.J., 2020. A convolutional neural network approach to deblending seismic data. Geophysics 85 (4), WA13–WA26. https://doi.org/10.1190/geo2019-0173.1.

Trickett, S.R., 2003. F-xy eigenimage noise suppression. Geophysics 68 (2), 751–759. https://doi.org/10.1190/1.1567245.

Wang, B., 2016. An efficient pocs interpolation method in the frequency-space domain. IEEE Geosci. Rem. Sens. Letters 13, 1384–1387. https://doi.org/10.1109/lgrs.2016.2589260.

Wang, B., Zhang, N., Lu, W., Wang, J., 2019. Deep-learning-based seismic data interpolation: A preliminary result. Geophysics 84 (1), V11–V20. https://doi.org/10.1190/geo2017-0495.1.

Wang, Z., Bovik, A.C., Sheikh, H.R., Simoncelli, E.P., 2004. Image quality assessment: From error visibility to structural similarity. IEEE Trans. Image Process. 13, 600–612. https://doi.org/10.1109/tip.2003.819861.

Woo, S., Park, J., Lee, J.Y., Kweon, I.S., 2018. CBAM: Convolutional block attention module. In: Proceedings of the European Conference on Computer Vision. ECCV, pp. 3–19. https://doi.org/10.48550/arXiv.1807.06521.

Wu, X., Geng, Z., Shi, Y., Pham, N., Fomel, S., Caumon, G., 2020. Building realistic structure models to train convolutional neural networks for seismic structural interpretation. Geophysics 85 (4), WA27–WA39. https://doi.org/10.1190/geo2019-0375.1.

Wu, X., Liang, L., Shi, Y., Fomel, S., 2019a. Faultseg3D: Using synthetic data sets to train an end-to-end convolutional neural network for 3D seismic fault segmentation. Geophysics 84 (3), IM35–IM45. https://doi.org/10.1190/geo2018-0646.1.

Wu, X., Ma, J., Si, X., Bi, Z., Yang, J., Gao, H., Xie, D., Guo, Z., Zhang, J., 2023. Sensing prior constraints in deep neural networks for solving exploration geophysical problems. Proc. Natl. Acad. Sci. 120, e2219573120. https://doi.org/10.1073/pnas.2219573120.

Wu, X., Shi, Y., Fomel, S., Liang, L., Zhang, Q., Yusifov, A.Z., 2019b. Faultnet3D: predicting fault probabilities, strikes, and dips with a single convolutional neural network. IEEE Trans. Geosci. Rem. Sens. 57, 9138–9155. https://doi.org/10.1109/tgrs.2019.2925003.

Wu, X., Yan, S., Bi, Z., Zhang, S., Si, H., 2021. Deep learning for multidimensional seismic impedance inversion. Geophysics 86 (5), R735–R745. https://doi.org/10.1190/geo2020-0564.1.

Xu, K., Ba, J., Kiros, R., Cho, K., Courville, A., Salakhudinov, R., Zemel, R., Bengio, Y., 2015. Show, attend and tell: Neural image caption generation with visual attention. In: International Conference on Machine Learning, PMLR, pp. 2048–2057. https://doi.org/10.48550/arXiv.1502.03044.

Yu, J., Wu, B., 2021. Attention and hybrid loss guided deep learning for consecutively missing seismic data reconstruction. IEEE Trans. Geosci. Rem. Sens. 60, 5902108. https://doi.org/10.1109/tgrs.2021.3068279.

Zhang, G., Duan, J., Li, Y., He, C., Du, H., Luo, F., Zhan, Y., Wang, J., 2020. Adaptive time-resampled high-resolution synchrosqueezing transform and its application in seismic data. IEEE Trans. Geosci. Rem. Sens. 58, 6691–6698. https://doi.org/10.1109/tgrs.2020.2978509.

Zhang, H., Li, Y., Huang, J., 2024. Conditional denoising diffusion probabilistic model for seismic diffraction separation and imaging. IEEE Trans. Geosci. Rem. Sens. 62, 5912413. https://doi.org/10.1109/tgrs.2024.3381193.

Zhu, W., Mousavi, S.M., Beroza, G.C., 2019. Seismic signal denoising and decomposition using deep neural networks. IEEE Trans. Geosci. Rem. Sens. 57, 9476–9488. https://doi.org/10.1109/tgrs.2019.2926772.